Nocturnal Aerosol Optical Depth Measurements with a Small-Aperture Automated Photometer Using the Moon as a Light Source

TIMOTHY A. BERKOFF

University of Maryland, Baltimore County, Baltimore, Maryland

MIKAIL SOROKIN

Sigma Research Inc., Lanham, Maryland

TOM STONE

United States Geological Survey, Flagstaff, Arizona

THOMAS F. ECK AND RAYMOND HOFF

University of Maryland, Baltimore County, Baltimore, Maryland

ELLSWORTH WELTON AND BRENT HOLBEN

NASA Goddard Space Flight Center, Greenbelt, Maryland

(Manuscript received 18 November 2010, in final form 5 April 2011)

ABSTRACT

A method is described that enables the use of lunar irradiance to obtain nighttime aerosol optical depth (AOD) measurements using a small-aperture photometer. In this approach, the U.S. Geological Survey lunar calibration system was utilized to provide high-precision lunar exoatmospheric spectral irradiance predictions for a ground-based sensor location, and when combined with ground measurement viewing geometry, provided the column optical transmittance for retrievals of AOD. Automated multiwavelength lunar measurements were obtained using an unmodified Cimel-318 sunphotometer sensor to assess existing capabilities and enhancements needed for day/night operation in NASA's Aerosol Robotic Network (AERONET). Results show that even existing photometers can provide the ability for retrievals of aerosol optical depths at night near full moon. With an additional photodetector signal-to-noise improvement of 10–100, routine use over the bright half of the lunar phase and a much wider range of wavelengths and conditions can be achieved. Although the lunar cycle is expected to limit the frequency of observations to 30%–40% compared to solar measurements, nevertheless this is an attractive extension of AERONET capabilities.

1. Introduction

Atmospheric aerosols represent the greatest uncertainty in determining key questions in radiative energy balance for climate change (Solomon et al. 2007) and have important relationships to air quality (Pope et al. 2002), atmospheric chemistry (Andreae and Crutzen 1997), and cloud formation (Kaufman and Koren 2006). Several satellite programs and their resultant data products provide the ability to study long-term aerosol optical depth (AOD) characteristics on a global scale; examples include the Moderate Resolution Imaging Spectroradiometer (Remer et al. 2005), Multiangle Imaging Spectroradiometer (Kahn et al. 2005), Geostationary Operational Environmental Satellite (GOES) Aerosol Smoke Product (Prados et al. 2007), Sea-viewing Wide Field-of-view Sensor (Wang et al. 2000), and Cloud-Aerosol lidar and Infrared Pathfinder Satellite Observation (CALIPSO; Winker et al. 2007). Surface-based measurement capabilities include the development of photometers to provide columnar AOD measurements (Voltz 1959; Shaw and Deehr 1975; O'Neill and

Corresponding author address: Timothy A. Berkoff, NASA GSFC, Code 613.1, Greenbelt, MD 20771.
E-mail: berkoff@umbc.edu

DOI: 10.1175/JTECH-D-10-05036.1

© 2011 American Meteorological Society

Miller 1984; Dutton et al. 1994) and the National Aeronautics and Space Administration's (NASA) formation of the Aerosol Robotic Network (AERONET), a worldwide network of photometers with over 300 partner sites around the globe (Holben et al. 1998, 2001). AERONET provides a mechanism for the standardization of instruments, calibration, and centralized processing of data yielding a long-term, continuous, and readily accessible public domain database of aerosol optical, microphysical, and radiative properties for aerosol research, and characterization and validation of satellite retrievals (Chu et al. 2002; Kaufman et al. 2001; Eck et al. 2009). With the exception of active sensor measurements such as lidar systems (Winker et al. 2007; Pappalardo et al. 2010; Welton et al. 2001), large-scale global records of AOD transmittance are limited to passive measurements relying on illumination from the sun. Consequently, nocturnal multiwavelength AOD records are limited in scope, but nevertheless remain a subject of ongoing interest (Zhang et al. 2008). To better understand the diurnal behavior of aerosols, preconvection, and prephotochemistry effects, and nocturnal mixing layer dynamics, nighttime AOD measurements are necessary. In particular, high-latitude locations experience extended periods of darkness during winter, where nighttime AOD capability would help address the largest temporal gaps in observations that rely on the sun (Eck et al. 2009; Stone et al. 2008; Tomasi et al. 2007). Such data would also be expected to contribute to aerosol transport modeling efforts, either by assimilation or in validation studies. Furthermore, lidar programs such as CALIPSO (Winker et al. 2007) and NASA's Micropulse lidar Network (MPLNET; Welton et al. 2001) generate aerosol lidar data products that depend on underlying assumptions associated with the extinction-to-backscatter ratio for aerosol layers. Nighttime columnar AOD input for these programs would provide an additional constraint that could be used to improve nighttime aerosol backscatter and extinction data products.

Research groups have previously pursued ground-based photometers relying on passive measurements of the moon and stars as a means to obtain nighttime AODs (Herber et al. 2002; Esposito et al. 1998; Pérez-Ramírez et al. 2008). Early studies favored stellar over lunar measurements because of the challenges of using the moon as a light source, despite the added size, expense, and complexity of the large-aperture instrumentation needed to collect sufficient starlight. Although proven to be effective at determining nighttime AODs, stellar measurements are still limited in use, and no large-scale network has emerged comparable to AERONET in its automation and widespread locations around the globe. While the moon's photometric properties are virtually invariant ($<10^{-8}$ yr^{-1}; Kieffer 1997), the changing lunar brightness due to phase, the lunar librations, spatial nonuniformity, and non-Lambertian reflectance properties presents complexities in the radiant energy seen from Earth (Kieffer and Wildey 1996). However, provided the availability of such determinations, the significantly greater lunar brightness offers the potential to use small-aperture, simple photometers for nighttime AOD retrievals.

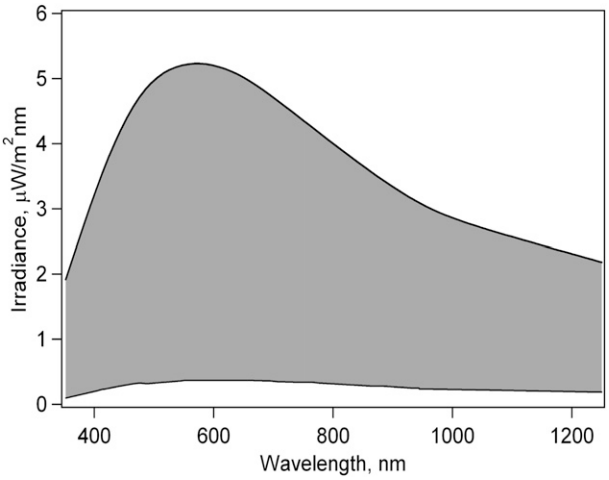

FIG. 1. Nominal range in lunar spectral irradiance (gray region) at the surface of Earth for full moon to quarter phase (0.5 disk illumination).

2. General approach

The plot in Fig. 1 displays a nominal range in values for lunar exoatmospheric irradiance between the first and third quarter ($\pm 90°$ lunar phase from full) received at Earth's location. Although this range is from $\sim 10^{-5}$ to 10^{-6} the irradiance of the sun, it is more than four orders of magnitude greater that the brightest star, Sirius. For a 1-cm-diameter aperture, a 10-nm spectral bandwidth in the visible range (0.4–1.0 μm), 0.5 atmospheric optical transmission, and 0.1 detector quantum efficiency, the photodetected power would be greater than 10^{-11} W, more than three orders of magnitude above conventional silicon photodiode noise-equivalent power detection limits (Ohno 1997). Thus small-aperture photometric measurements of the moon for AOD retrievals can be realistically achieved consistent with existing AERONET infrastructure and methodology for long-term aerosol observations.

The method employed here obtains the lunar source intensity from the U.S. Geological Survey (USGS) program for lunar calibration, known as the Robotic Lunar Observatory (ROLO). ROLO is a NASA-funded

program to provide the moon for on-orbit calibration of Earth Observing System (EOS) satellite instruments. To accomplish this, ROLO has developed a model for the lunar spectral irradiance (Kieffer and Stone 2005) based on extensive telescopic observations acquired over more than 8 yr. The ROLO model output has a relative precision of 1% or better over its full valid range of phase angles, eclipse to 90°. The lunar calibration system provides the irradiance of the moon for the precise time and location of a spacecraft instrument, in the instrument's spectral bands. This same capability can provide the top-of-atmosphere lunar irradiance at the location of a ground-based instrument. The current AOD study represents the first time the ROLO system has been used in this way.

Figure 2 displays the conceptual block diagram of the approach to retrieve AODs. After initial setup to establish the lunar source spectral interpolation to the photometer instrument bands, the ROLO system accepts inputs of geolocation (J2000 coordinates) and instrument-measured irradiance, in user-prepared formatted ASCII files. Processing these input files and generating model results is done interactively at USGS, although a Web services interface is under development. Nonetheless, the turnaround of results is rapid. Along with details of the lunar observation geometry, the ROLO system reports the percent difference between the instrument-measured and model-predicted irradiance for each band. For a ground-based instrument, this corresponds to the atmospheric transmission loss, which can be converted to a zenith optical depth by accounting for the air mass during an observation.

3. Calibration and AOD calculation

Although not intended for lunar observations, the photometer used in this demonstration is a standard Cimel Electronic sunphotometer (Model CE-318), with ~10 nm wide spectral passbands at 440, 500, 675, 870, 937, 1020, and 1246 nm. The 1246-nm filter channel uses an InGaAs detector while the other channels rely on a separate silicon detector. Both silicon and InGaAs detector channels are coaligned and each have a full-angle field of view (FOV) corresponding to 1.2°. An internal filter wheel allows automated rotation through multiple spectral filters to obtain multiwavelength measurements. This model sensor and the channel wavelengths are the same as utilized in AERONET, and they have a robust operational history and known calibration performance. There are three gain modes for the photodiode circuit that allow for direct sun, and two additional (higher gain) settings for sky brightness, which are utilized for aureole and almucantar measurements for higher-level microphysical retrievals. For lunar measurements in this work, the highest gain setting was used, corresponding to sky radiance measurements (away from sun) used for daytime operations, and corresponding to $\sim 4 \times 10^3$ increased gain over the direct sun gain setting.

The lunar irradiance E_λ for a given measurement was calculated from raw detector signal V_λ by

$$E_\lambda = k_\lambda (V_\lambda - D_\lambda), \tag{1}$$

where k_λ is the calibration coefficient and D_λ is the contribution from background and detector dark signal, with λ representing a particular spectral passband. The values for k_λ can be determined from different calibration techniques, either by the Langley method, cross-calibration with an existing reference sensor, or by a laboratory-based integrating sphere calibration. For this study, initial calibration values were estimated from a standard AERONET procedure for photometer radiance calibration using a laboratory-based integrating sphere. As a result, coefficients k_λ were calculated from

$$k_\lambda = L_\lambda \Omega, \tag{2}$$

where L_λ values are photometer radiance responsivity in μW (V sr nm m^2)$^{-1}$ and Ω is the solid angle of 0.34×10^{-3} sr, corresponding to the photometer field of view as reported by the manufacturer. The laboratory-based calibration procedure provides radiance (L_λ) values to $\pm 5\%$ accuracy. The approach is nonideal because of instrumental factors in the radiance–irradiance conversion, but nevertheless provides a useful first estimate of the photometer responsivity. In the future, this initial calibration could be refined with a more formal mountaintop Langley calibration following standard AERONET methodology, or collocated stellar reference measurement. In addition, the 937-nm channel for water vapor and a 1246-nm channel (from the InGaAs detector) were not calibrated directly from the sphere, since this required a nonstandard read-out sequence that was not available at the time of calibration. Nominal values for these two channels were estimated from typical characteristic responses known for this type of photometer. Table 1 displays the k_λ values used for each of the photometer wavelength channels. During lunar observations, background D_λ values are determined by recording sky measurements tipped 4° away from the moon immediately after recording V_λ signals aligned to the moon. Once E_λ values are calculated from (1) for a given series of nighttime measurements, exchange input files were prepared for ROLO model input. The ROLO algorithm calculates the expected lunar irradiance E'_λ for each of the observations (free of atmospheric

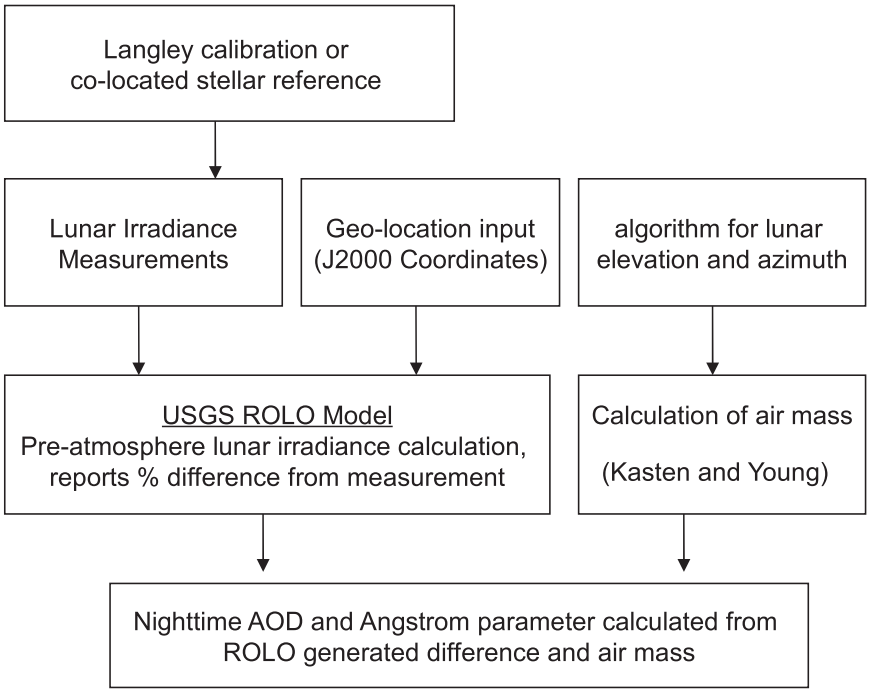

FIG. 2. Block diagram for the generation of nighttime AOD using the USGS ROLO model.

attenuation). These calculations included input parameters of the manufacturer-supplied spectral band transmittance curves for each the sensor bandpass filters. The ROLO output reports the percent difference between the user-supplied surface E_λ measurements and the model-generated E'_λ:

$$R_{\%} = 100(E_\lambda - E'_\lambda)/E'_\lambda. \quad (3)$$

Rearranging in terms of fractional atmosphere transmittance, this becomes

$$E_\lambda/E'_\lambda = 1 + R_{\%}/100, \quad (4)$$

noting that $R_{\%}$ values are negative values yielding transmittance values less than 1.

Of interest here is the calculation of aerosol optical depths for all filter channels for each of the surface observations. In simplified form, the atmosphere transmittance is given by the well-known Beer–Lambert–Bouger law,

$$E_\lambda/E'_\lambda = \exp[-(\tau_\alpha + \tau_r)m], \quad (5)$$

where for each channel τ_a and τ_r are the spectral aerosol and Rayleigh optical depths, respectively, and m is the relative air mass determined from the lunar zenith angle Θ_z utilizing the Kasten and Young (1989) formalism, repeated here for convenience:

$$m = \frac{1}{\cos(\Theta_Z) + \left[\dfrac{0.505\,720}{(96.079\,950 - \Theta_Z)^{1.636\,40}}\right]}. \quad (6)$$

Equating (4) and (5) and solving for τ_a, the aerosol optical depth for a given filter channel was directly calculated from ROLO return $R_{\%}$ values by

$$\tau_a = \frac{\ln\left(1 + \dfrac{R_{\%}}{100}\right)}{-m} - \tau_r, \quad (7)$$

where values for the contribution of Rayleigh optical depth τ_r were obtained from prior work (Bucholtz 1995) based on standard midlatitude atmosphere criteria. For

TABLE 1. Calibration values (±5% accuracy) used to calculate irradiance from raw signal voltages.

ch λ (nm)	k_λ [μW (V sr nm m^2)$^{-1}$]
440	0.042
500	0.021
675	0.015
870	0.014
937	0.017*
1020	0.020
1246	0.0092*

* Values not from integrating sphere calibration.

870-nm and longer wavelengths, it is assumed $\tau_r = 0$. Additionally, attenuation due to molecular absorption (i.e., ozone, NO_2) was neglected in these calculations, as it has a relatively small effect <0.015 AOD (Eck et al. 1999).

4. Photometer setup and operation

The Cimel photometer was set up on the rooftop of the University of Maryland, Baltimore County (UMBC) physics building located in Baltimore, Maryland (39.25°N, 76.71°W) for automated measurements of lunar irradiance. This site was attractive because of the clear line of sight to the horizon, and is host to a variety of atmospheric instruments supported by the UMBC Monitoring of Atmospheric Pollution (UMAP) program, including a Cimel sunphotometer participating in AERONET and a micropulse lidar system participating in MPLNET, in addition to a variety of aerosol surface characterization instruments. The standard commercial control interface box for the Cimel-318 photometer contains a firmware system that automatically tracks the sun and records measurements. To enable customization for lunar tracking and measurements, the sensor head was mounted to a two-axis motor stage that provided 0.01° high-precision control in both elevation and azimuth. Both the sensor head and the motor stage were interfaced to a laptop computer in environmental housing adjacent to the sensor that enabled automatic control over serial links using a custom software algorithm written in Python programming language.

For normal sun operations, the Cimel photometer first points to the approximate location of the sun and then utilizes a quadrant-tracking detector to optimize alignment for a maximum signal to center the instrument's field of view. In this study the quadrant sensor was not used because of insufficient gain for reliable lunar tracking, and instead a custom alignment algorithm was developed using a wideband signal available from one of the photometer filter wheel positions. The first step of the alignment algorithm utilized a lookup table of topocentric azimuth and elevation coordinates generated from the U.S. Naval Observatory Multiyear Interactive Computer Almanac (MICA) to provide a rough orientation of the sensor view angle to the moon. The second stage of the procedure sweeps the sensor-pointing angle over a sky circular area of 3° radius to find the maximum signal location. The circle sweep area progressively decreases in size with a final tuning of the position in 0.01° steps, a process that takes approximately 35 s. After finalizing to the maximum signal position, the photometer is momentarily pointed 4° away to obtain a background measurement. If the maximum signal meets a minimum raw signal threshold and is 3 times greater than the background level, the new coordinate location is accepted as a valid alignment and raw data for all filter passbands are recorded.

To verify the functionality of the alignment algorithm, a laboratory benchtest was conducted to evaluate the angular repeatability of the procedure. The statistical results from a random trial of 20 alignment procedures were recorded for a small diameter lamp source that was placed at a distance (~1 m) away from the photometer to mimic the 0.5° angular size extent of the moon. Randomly generated angles between −2° and 2° were applied to the azimuth and elevation motor positions prior to each run. The resultant standard deviation in azimuth and elevation from this trial were 0.026° and 0.024°, respectively. These deviations are about 2 times larger than the motor step resolution of 0.013°, and ~1/40 the size of the FOV of the instrument. These findings were generally found to be consistent with short-term variability recorded during observations with respect to MICA predictions, indicating the alignment procedure was working effectively.

The software developed for this study provided fully automatic control of the motor position, photometer alignment, and multiwavelength measurements. A custom graphical user interface allowed for the real-time lookup of sun and moon positions, manual setup and test procedures, and parameter entry for measurement frequency during automated measurements. In automated mode, observation start and stop times were obtained from a predetermined multimonth schedule file generated from MICA-predicted coordinates for the sun and moon. The system automatically switched photodetector gain as needed between sun and moon observations, utilizing the same alignment and multiwavelength recording procedure for both day and night. Motor position offsets relative to the expected MICA azimuth and elevation were recorded for each alignment, along with alignment stability statistics, background measurements, and other system housekeeping information. Initial automated data collection testing started in December 2009, with software improvements implemented in February 2010 providing automated measurements on various evenings through July 2010. From the photometer dataset, two representative cases are described in detail here to illustrate AOD retrievals under low- and high-AOD conditions.

5. Results

a. 1 February low-AOD case study

The first case examined lunar data obtained on the morning of 1 February 2010 for a waning moon with

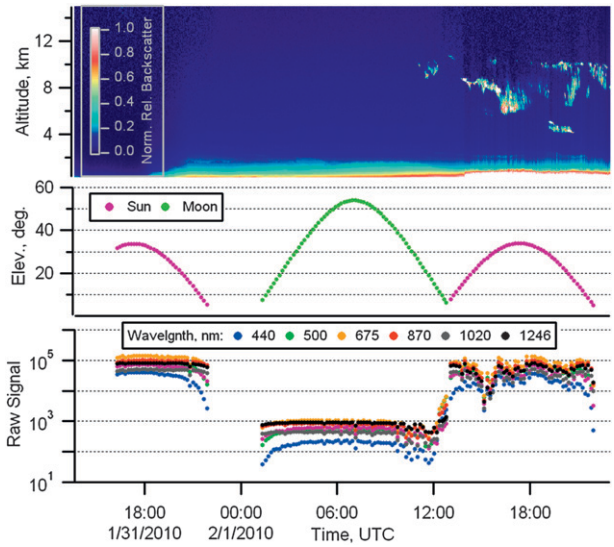

FIG. 3. (top) Normalized relative backscatter lidar data, (middle) sun and moon elevations, and (bottom) multiwavelength lunar irradiance measurements.

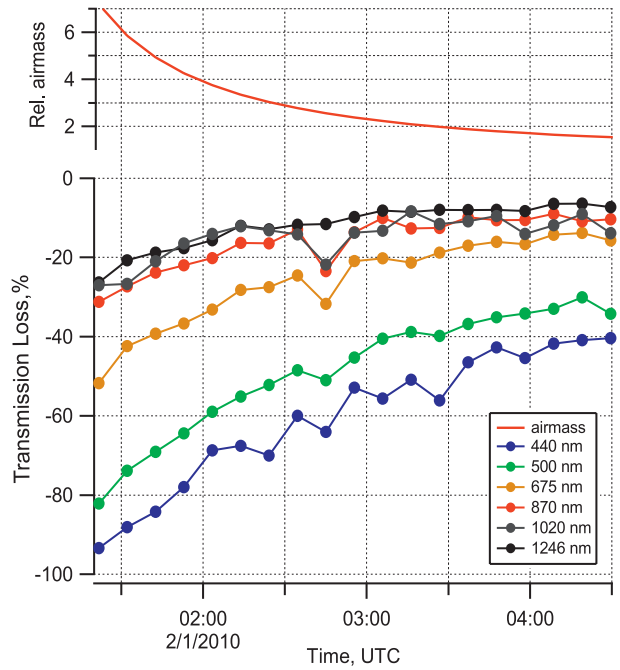

FIG. 4. (top) Data segment selected for Langley analysis with air mass and (bottom) return calculations from ROLO processing reporting the percent transmission loss for each of the photometer wavelengths.

~0.9 fractional disk illumination. This segment was selected because of relatively stable atmospheric conditions that occurred between the day/night transition, and provided the best Langley calibration opportunity in the data obtained to date. Data from the collocated micropulse lidar system provided MPLNET level-1.0 normalized relative backscatter (NRB) intensity profiles for the qualitative assessment of aerosol and cloud features during the course of measurements. Figure 3 displays the NRB image at 527-nm wavelength from the MPL system before, during, and after lunar measurements, along with sun and moon elevation angles, and the multiwavelength raw signal magnitudes from the photometer. Automated measurements included both the sun and moon raw-signal magnitudes as shown, with each data point representing the mean of four concurrent 150-ms time measurements in series to provide a total 600-ms time-averaged value for each wavelength band. The lidar data indicate that relatively stable, cloud-free sky conditions existed prior to sunset on 31 January, and continued through the 1 February moonrise, with cirrus clouds appearing later in the morning just before sunrise. The photometer observations for all wavelengths were collected on a 10-min interval for the sun and moon. Even with the detector gain increase of 4000 when using the sky gain setting for the moon, the raw digital values from the photometer are about two orders of magnitude smaller than the sun, consistent with expected relative change in irradiance levels. During sunset and moonrise, the increased attenuation due to air mass is apparent and can be distinctly resolved for all wavelengths. The signal behavior remains relatively stable after moonrise until later in the day when cirrus clouds appear over the site, causing temporal variability in the recorded photometer signal magnitudes.

Using the calibration coefficients from Table 1, 1 February raw lunar data were converted to irradiance values E, from which ROLO ingest files were generated. Values returned from ROLO provided the percent difference from model predictions to measured irradiance at the surface, $100(E_\lambda - E'_\lambda)/E'_\lambda$, representing the loss due to the atmosphere. Figure 4 shows a subset of data between 0121 and 0429 UTC when the lunar air mass ranged from 7 to 1.5. This segment was selected for Langley analysis and is displayed in Fig. 5, with the linear regression slopes yielding the atmosphere total optical depth ($\tau_m + \tau_p$) and the y-axis intercepts ideally being zero (where $E/E_0 = 1$), indicating closure on the exoatmosphere lunar irradiance. Error in the y intercepts ranged from 0.071 to −0.057, with the greatest deviations exhibited by the 440- (0.071) and 1020-nm channels (−0.057). The 1020-nm channel for these systems exhibits a temperature dependence due to the long-wavelength cutoff response that was not available for this specific photometer and requires temperature chamber testing. Results presented here include a representative correction (0.3% °C^{-1} in irradiance) based

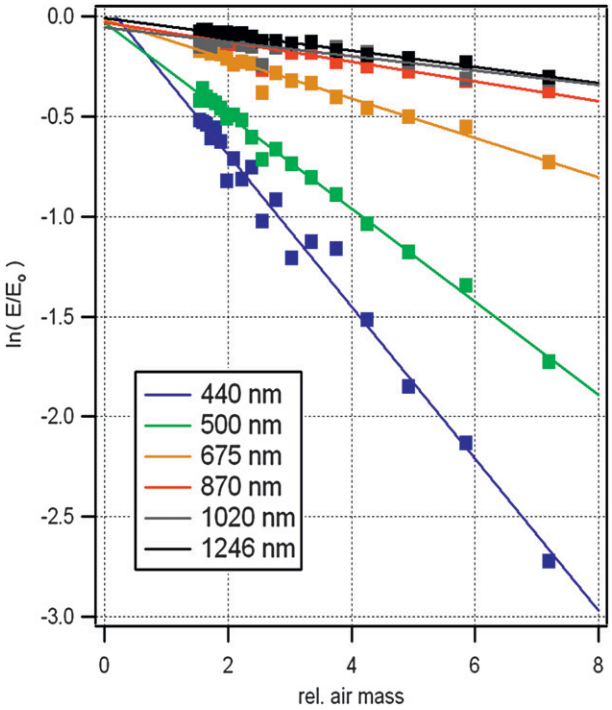

FIG. 5. Langley analysis of the 1 Feb data from Fig. 4, with linear regression fits (solid lines) to independently determine optical depths.

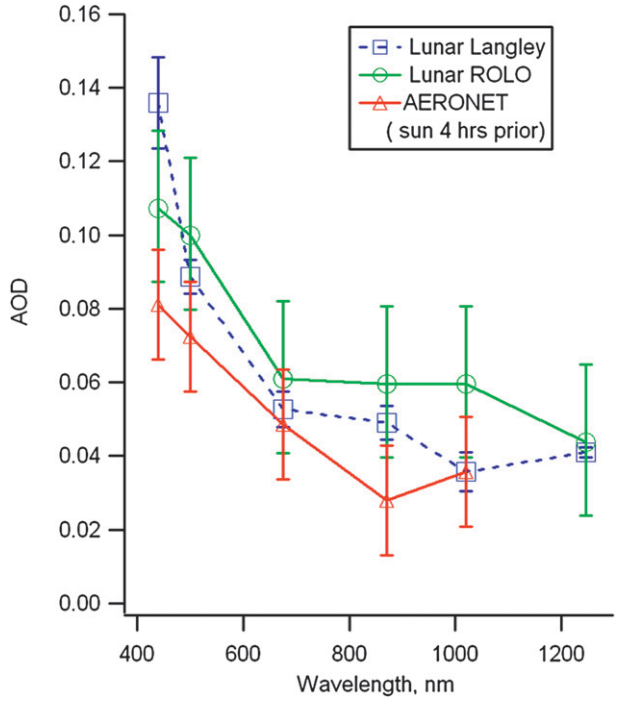

FIG. 6. Multiwavelength AOD determinations from 1 Feb data segment, comparing direct ROLO return calculations (circles), Langley analysis (squares), and sunphotometer-reported values (triangles) 4 h prior to the lunar data segment (mean values of last hour of available sun data).

on composite data from several systems that underwent thermal chamber characterization and the temperature values as reported by the Cimel sensor during observations. The remaining channel intercept differences were 0.03 or less, which is consistent with the known absolute error from integrating sphere calibration. Additionally, this particular Langley analysis occurred in nonideal atmospheric conditions, as AERONET calibrations are normally conducted at a high-altitude mountaintop facility in the free troposphere, to reduce corruption by aerosol temporal instabilities. Nevertheless, these results are useful for an initial assessment, as the Langley data could be used to reduce further absolute errors associated with residual bias from the initial calibration.

Figure 6 compares the calculated AODs obtained from Langley analysis, the calculated mean AOD from (7) using direct lunar measurements during the same time interval as the Langley analysis, and solar-determined AOD measurements from AERONET (1.5-level data) from an independent collocated photometer. The AERONET sun data are mean values for the last hour of observations that ended ~3.5 h prior to the lunar observations. During this time, the lidar data indicate relatively stable atmospheric conditions, thus sun data taken 3.5 h prior provide an additional reference point for comparisons. The error bars for the direct lunar AOD values (ROLO) represent the 5% absolute radiance corresponding to the laboratory-based integrating sphere calibration, the lunar Langley analysis errors were obtained from the slope uncertainties from the regression analysis, and sunphotometer AOD error bars represent maximum calibration error expected for AERONET level-1.5 data (Eck et al. 1999). AODs show general agreement with the characteristic decline in attenuation with increasing wavelength although both the direct and Langley-retrieved AODs from the moon have a high bias relative to the daytime AERONET observations. Contributions from NO_2 and O_3 absorption were not specifically corrected in this initial demonstration, and would be expected to contribute to the slight high bias seen in the results. The discrepancies between lunar Langley and ROLO results are of the order of those between lunar Langley and AERONET. The exact cause of these discrepancies cannot be determined from this study, but they are not surprising given the calibration limitations of this initial work.

b. 31 May pollution event—high-AOD case study

On 31 May 2010, a significant increase in aerosol entered the region at night that resulted in the U.S.

Environmental Protection Agency issuing code orange (unhealthy for sensitive groups) to red (unhealthy) warnings for the Northeast for the following days. This aerosol event was attributed to a combination of pollution from the Midwest and smoke transported from Quebec, Canada, forest fires to the north. A waning moon with a disk illuminated fraction of 0.9 enabled lunar measurements to be recorded during this event, capturing the nocturnal AOD transition. Figure 7 displays the 527-nm NRB intensity from the lidar, the AERONET level-1.5 sunphotometer data before and after the nighttime transient, and AODs derived from lunar measurements (taken at 2-min intervals) using the same calibration and methodology as the low-AOD case study. Because of noise levels, the lunar data are fitted with a 5-point boxcar smoothing average (solid lines) to better reveal the signal trend. Also displayed are the AOD standard deviations propagated from recorded irradiance uncertainties during measurements for each of the lunar observations, similarly fitted with a 5-point boxcar average. The lidar backscatter data provide height and temporal features of the aerosol intensification, during and in between the sun and lunar observations, although only at the single wavelength of 527 nm. As can be seen in the level-1.5 AERONET results, low AODs (<0.1 at 440 nm) just prior to sunset occurred the day before, and high AOD (~0.5 at 440 nm) just after sunrise on 31 May. Lunar data collection started ~4 h after the last available sun data on 30 May and stopped ~1 h prior to the next available sun data on the following day, 31 May. The lunar AOD values in between the sun observations captured the aerosol intensification, qualitatively consistent with the increase in aerosols as seen by the lidar. However, the 440-nm channel exhibited a false-high artifact during the first hour (0400–0500 UTC), when atmospheric attenuation exceeded 80% because of high air mass at the beginning of moonrise. AOD uncertainties during these observations were propagated from the measured irradiance standard deviations resulting from the dark noise limit of the post-photodiode electronics. For this case, this translated to the 440-nm channel exhibiting a mean AOD standard deviation of 0.2, with the remaining longer wavelength channels having a significantly better performance ranging from 0.01 to 0.04 AOD.

Because of the aerosol dynamics, Langley analysis is not possible in this case as an independent assessment of calibration. The closest night/day cross-comparison reference points occur at the end of lunar measurements (0918 UTC) and the start of solar measurements 1.5 h later. The 15-min mean solar and lunar AODs closest in time to this night/day transition are displayed as a correlation plot in Fig. 8. The values span from 0.1 to 0.5 with the lower AODs corresponding to the longer wavelengths. Also included are the data from the 1 February (low-AOD case) day/night transition that span over a much smaller and lower AOD range. As can be seen, lunar-derived AODs tend to exhibit a high bias relative to sun data that is more pronounced at the longer wavelength channels. These residual calibration differences would need to be addressed in a more extensive calibration study, ideally following well-established high-altitude Langley analysis procedures over a range of lunar phase angles, to extend this initial work toward broader use within AERONET.

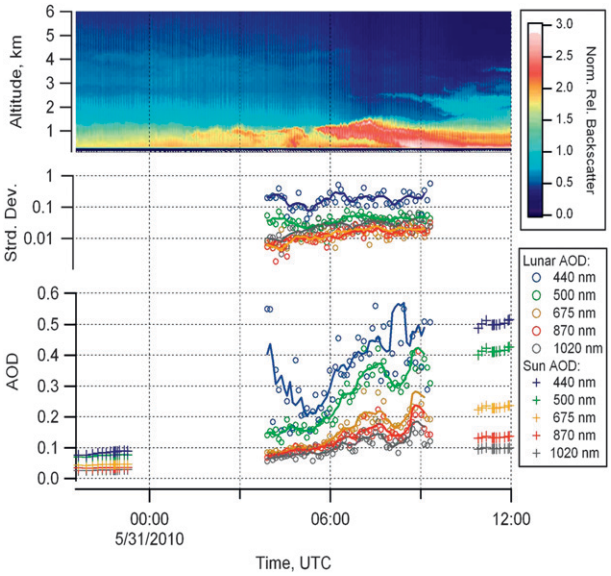

FIG. 7. High-AOD case on 31 May, with (top) lidar normalized relative backscatter profiles, (bottom) sun (+) and lunar (o) AOD values, and (middle) lunar AOD standard deviations. Because of noise levels, lunar data are fitted with a 5-point boxcar smoothing function (solid lines) to better reveal the aerosol trend.

6. Discussion and conclusions

Despite the inherent complexities in using lunar irradiance for nighttime measurements of AOD, it is possible to obtain nighttime AOD using a small-aperture photometer similar to those used in AERONET. This was enabled by the use of the USGS ROLO model to provide high-precision lunar irradiance for a fixed ground-based location, and when combined with ground-based photometer measurements, atmospheric columnar multiwavelength AODs were obtained for the first time using this approach. While this initial demonstration relied on an unmodified Cimel sunphotometer never designed for lunar measurements, automated lunar alignment and measurements were nevertheless achieved for near-full moon conditions over a range of AODs when using the sky gain setting of the photometer.

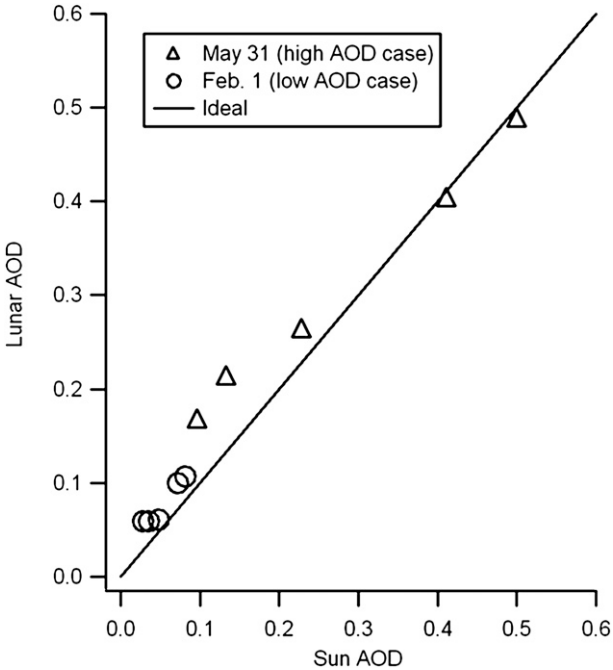

FIG. 8. Correlation plot of AOD lunar values closest in time to AOD solar values for 31 May high-AOD case (triangles) and 1 Feb low-AOD case (circles).

The data collected in this study provide a limited examination of the approach because of larger than desired (±5%) systematic error in the laboratory-based calibration for this work. ROLO provides <1% irradiance precision and repeatability that is sufficient for desired AOD performance goals; however, residual systematic offset differences between ROLO and instrument irradiance values would need to be further evaluated. This could be accomplished with measurements in the free troposphere at the Mauna Loa calibration facility routinely used by AERONET, which would provide additional Langley analysis opportunities and enable closure with ROLO irradiances. Similarly, collocated stellar reference measurements could also be used to identify systematic differences and further validate the methodology of this technique. In either approach, it would be desirable to evaluate systematic differences over a range of lunar phase conditions that are not available in this initial study.

A key limitation in this study was electronic noise of the sensor circuit, and does not represent a fundamental noise limit of silicon photodiode detection capabilities. To improve performance, an increase in signal-to-noise by a factor of 10–100 is desired to extend detection capabilities to more closely reach standard AERONET performance over the bright half of lunar phase angles (±90° about full) for a range of AODs and air masses needed for broad application. With the random noise and systematic uncertainties reduced below 1% irradiance, this method would then approach the precision limit of the ROLO model output. When factoring in the lunar phase covered by ROLO, viewing geometries, and solar background, an observational frequency of 30%–40% is estimated as compared to solar observations on an annual basis. The seasonal day/night extent becomes more pronounced for higher latitudes, increasing lunar observations for winter and reducing them for summer.

As with solar AOD determinations, the number of observations for a given time interval would be reduced by the cloud fraction for a given site. For this study, we avoided using cloud-contaminated data for aerosol analysis since collocated lidar data were available. In a future implementation, AERONET cloud screening procedures would be applied to the nighttime data to avoid contamination of AOD data. Even with AERONET screening, it is still possible that some residual contamination could occur in cases such as stable thin cirrus layers not recognized by automated procedures. In these circumstances, more sophisticated algorithms would need to be employed to reduce these effects and a future study is planned with collocated lidar measurements to help identify such influences.

Although this approach has fewer observations compared to one using the sun, it is the closest in compatibility for existing AERONET infrastructure and can be applied to other ground-based sensors utilizing the moon for atmospheric and astronomy studies. In addition, lidar data streams from CALIPSO and MPLNET depend on instrument calibrations and underlying assumptions associated with the extinction-to-backscatter ratio to produce quantitative aerosol data. This additional columnar AOD capability provides input to help further improve lidar retrievals at nighttime, when signal-to-noise performance is at an optimum. By utilizing existing AERONET infrastructure, the extension to nighttime AOD measurements is expected to provide a range of useful benefits to aerosol studies, modeling efforts, and satellite retrievals. Since the initiation of this study, the photometer manufacturer, Cimel Electronique, is currently pursuing an improved sensor version that would enable automatic lunar tracking via the sunphotometer's built-in quadrant detector and improved signal output for use with the moon.

Acknowledgments. The authors wish to acknowledge Marius Canini (Cimel Eletronique), Nader Abuhassan (UMBC), and Joel Schafer (Sigma Research) for technical advice and assistance, and Patricia Sawamura (UMBC), Daniel Orozco (UMBC), and Alex Tran (Sigma Research) for photometer operational assistance.

This work was supported in part by the MPLNET, USGS ROLO, and UMBC Measurement of Atmospheric Pollution (UMAP) Baltimore Air Quality projects, funded by the NASA EOS and Radiation Sciences programs. Open source software used in this work includes Python programming language (http://www.python.org/) for instrumentation and data collection and Open Office (http://www.openoffice.org/) productivity suite for the preparation of figures and text. We thank the anonymous reviewers who helped to significantly improve the original manuscript.

REFERENCES

Andreae, M. O., and P. J. Crutzen, 1997: Atmospheric aerosols: Biogeochemical sources and role in atmospheric chemistry. *Science,* **276,** 1052–1058, doi:10.1126/science.276.5315.1052.

Bucholtz, A., 1995: Rayleigh-scattering calculations for the terrestrial atmosphere. *Appl. Opt.,* **34,** 2765–2773.

Chu, D. A., Y. J. Kaufman, C. Ichoku, L. A. Remer, D. Tanre, and B. N. Holben, 2002: Validation of MODIS aerosol optical depth retrieval over land. *Geophys. Res. Lett.,* **29,** 8007, doi:10.1029/2001GL013205.

Dutton, E. G., P. Reddy, S. Ryan, and J. Deluisi, 1994: Features and effects of aerosol optical depth observed at Mauna Loa, Hawaii: 1982-1992. *J. Geophys. Res.,* **99,** 8295–8306.

Eck, T. F., B. Holben, J. Reid, O. Dubovik, A. Smirnov, N. O'Neill, I. Slutsker, and S. Kinne, 1999: Wavelength dependence of the optical depth of biomass burning, urban, and desert dust aerosols. *J. Geophys. Res.,* **104** (D24), 31 333–31 349.

——, and Coauthors, 2009: Optical properties of boreal region biomass burning aerosols in central Alaska and seasonal variation of aerosol optical depth at an Arctic coastal site. *J. Geophys. Res.,* **114,** D11201, doi:10.1029/2008JD010870.

Esposito, F., C. Serio, G. Pavese, G. Auriemma, and C. Satriano, 1998: Measurements of nighttime atmospheric optical depth preliminary data from a mountain site in southern Italy. *J. Aerosol Sci.,* **29** (10), 1213–1218.

Herber, A., and Coauthors, 2002: Continuous day and night aerosol optical depth observations in the Arctic between 1991 and 1999. *J. Geophys. Res.,* **107,** 4097, doi:10.1029/2001JD000536.

Holben, B. N., and Coauthors, 1998: AERONET—A federated instrument network and data archive for aerosol characterization. *Remote Sens. Environ.,* **66,** 1–16.

——, and Coauthors, 2001: An emerging ground-based aerosol climatology: Aerosol optical depth from AERONET. *J. Geophys. Res.,* **106,** 12 067–12 097.

Kahn, R. A., B. J. Gaitley, J. V. Martonchik, D. J. Diner, K. A. Crean, and B. Holben, 2005: Multiangle Imaging Spectroradiometer (MISR) global aerosol optical depth validation based on 2 years of coincident Aerosol Robotic Network (AERONET) observations. *J. Geophys. Res.,* **110,** D10S04, doi:10.1029/2004JD004706.

Kasten, F., and A. T. Young, 1989: Revised optical air mass tables and approximation formula. *Appl. Opt.,* **28,** 4735–4738.

Kaufman, Y., and I. Koren, 2006: Smoke and pollution aerosol effect on cloud cover. *Science,* **313,** 655–658, doi:10.1126/science.1126232.

——, D. Tanre, O. Dubovik, A. Karnieli, and L. A. Remer, 2001: Absorption of sunlight by dust as inferred from satellite and ground-based remote sensing. *Geophys. Res. Lett.,* **28,** 1479–1482.

Kieffer, H., 1997: Photometric stability of the lunar surface. *Icarus,* **130,** 323–327.

——, and R. Wildey, 1996: Establishing the moon as a spectral radiance standard. *J. Atmos. Oceanic Technol.,* **13,** 360–375.

——, and T. C. Stone, 2005: The spectral irradiance of the moon. *Astron. J.,* **129,** 2887–2901.

Ohno, Y., 1997: Photometric standards. *Handbook of Applied Photometry,* C. DeCusatis, Ed., Optical Society of America, 55–98.

O'Neill, N., and J. R. Miller, 1984: Combined solar aureole and solar beam extinction measurements. *Appl. Opt.,* **23,** 3691–3704.

Pappalardo, G., and Coauthors, 2010: EARLINET correlative measurements for CALIPSO: First intercomparison results. *J. Geophys. Res.,* **115,** D00H19, doi:10.1029/2009JD012147.

Pérez-Ramírez, D., J. Aceituno, B. Ruiza, F. J. Olmo, and L. Alados-Arboledas, 2008: Development and calibration of a star photometer to measure the aerosol optical depth: Smoke observations at a high mountain site. *Atmos. Environ.,* **42,** 2733–2738.

Pope, C. A., III, R. T. Burnett, M. J. Thun, E. E. Calle, D. Krewski, K. Ito, and G. D. Thurston, 2002: Lung cancer, cardiopulmonary mortality, and long-term exposure to fine particulate air pollution. *J. Amer. Med. Assoc.,* **287,** 1132–1141, doi:10.1001/jama.287.9.1132.

Prados, A. I., S. Kondragunta, P. Ciren, and K. R. Knapp, 2007: GOES Aerosol/Smoke Product (GASP) over North America: Comparisons to AERONET and MODIS observations. *J. Geophys. Res.,* **112,** D15201, doi:10.1029/2006JD007968.

Remer, L. A., and Coauthors, 2005: The MODIS aerosol algorithm, products and validation. *J. Atmos. Sci.,* **62,** 947–973.

Shaw, G. E., and C. S. Deehr, 1975: A photoelectric coronameter for atmospheric turbidity studies. *J. Appl. Meteor.,* **14,** 1203–1205.

Solomon, S., D. Qin, M. Manning, M. Marquis, K. Averyt, M. M. B. Tignor, H. L. Miller Jr., and Z. Chen, Eds., 2007: *Climate Change 2007: The Physical Science Basis.* Cambridge University Press, 996 pp.

Stone, R. S., G. P. Anderson, E. P. Shettle, E. Andrews, K. Loukachine, E. G. Dutton, C. Schaaf, and M. O. Roman III, 2008: Radiative impact of boreal smoke in the Arctic: Observed and modeled. *J. Geophys. Res.,* **113,** D14S16, doi:10.1029/2007JD009657.

Tomasi, C., and Coauthors, 2007: Aerosols in polar regions: A historical overview based on optical depth and in situ observations. *J. Geophys. Res.,* **112,** D16205, doi:10.1029/2007JD008432.

Voltz, F., 1959: Photometer mit Sele-Photoelement zur spek-tralen Messung der Sonnenstrahlung und zur Bestimmmung. *Arch. Meteor. Geophys. Bioklimatol.,* **B10,** 100–131.

Wang, M., S. Bailey, and C. R. McClain, 2000: SeaWiFS provides unique global aerosol optical property data. *Eos, Trans. Amer. Geophys. Union,* **81,** 197–202.

Welton, E. J., J. R. Campbell, J. D. Spinhirne, and V. S. Scott, 2001: Global monitoring of clouds and aerosols using a network of micro-pulse lidar systems. *Lidar Remote Sensing for Industry and Environmental Monitoring,* U. N. Singh, T. Itabe, and N. Sugimoto, Eds., International Society for Optical Engineering (SPIE Proceedings, Vol. 4153), 151–158.

Winker, D. M., W. H. Hunt, and M. J. McGill, 2007: Initial performance assessment of *CALIOP*. *Geophys. Res. Lett.,* **34,** L19803, doi:10.1029/2007GL030135.

Zhang, J., S. Reid, S. D. Miller, and F. J. Turk, 2008: Strategy for studying nocturnal aerosol optical depth using artificial lights. *Int. J. Remote Sens.,* **29,** 4599–4613.